Phase behavior of dipolar hard and soft spheres

Antti-Pekka Hynninen and Marjolein Dijkstra
Soft Condensed Matter, Debye Institute, Utrecht University, Princetonplein 5, 3584 CC Utrecht, The Netherlands
(Received 25 August 2005; published 30 November 2005)

We study the phase behavior of hard and soft spheres with a fixed dipole moment using Monte Carlo simulations. The spheres interact via a pair potential that is a sum of a hard-core Yukawa (or screened-Coulomb) repulsion and a dipole-dipole interaction. The system can be used to model colloids in an external electric or magnetic field. Two cases are considered: (i) colloids without charge (or dipolar hard spheres) and (ii) colloids with charge (or dipolar soft spheres). The phase diagram of dipolar hard spheres shows fluid, face-centered-cubic (fcc), hexagonal-close-packed (hcp), and body-centered-tetragonal (bct) phases. The phase diagram of dipolar soft spheres shows, in addition to the above mentioned phases, a body-centered-orthorhombic (bco) phase, and is in agreement with the experimental phase diagram [Nature (London) **421**, 513 (2003)]. In both cases, the fluid phase is inhomogeneous but we find no evidence of a gas-liquid phase separation. The validity of the dipole approximation is verified by a multipole moment expansion.

DOI: 10.1103/PhysRevE.72.051402 PACS number(s): 82.70.Dd, 64.70.−p, 83.80.Gv

I. INTRODUCTION

Colloidal particles in an external electric or magnetic field whose dielectric constant or magnetic susceptibility is different from that of the solvent, acquire a (electric or magnetic) dipole moment parallel to the field. The behavior of the colloids is governed by the dipole-dipole interaction, whose strength can be tuned by the magnitude of the field. Due to their unique shearing properties, such suspensions are called electrorheological (ER) and magnetorheological (MR) fluids. ER/MR fluids have potential use in industrial applications as hydraulic valves, clutches, brakes [1], and displays [2]. Moreover, the possibility to tune the crystal structure of these suspensions by an external field, makes these suspensions appealing for photonic applications [3–5].

The equilibrium structure of these fluids has been the subject of many experimental [3,4,6–8], theoretical [9–15], and simulation studies [16–20]. In an early theoretical study, Tao *et al.* proposed that above a certain critical field strength the system experiences a phase transition to a solid structure [9]. In Ref. [10], Tao and Sun studied the crystal structure of the solid phase and found that, of the structures that they considered, a body-centered-tetragonal (bct) structure was the one with the lowest energy. The bct structure predicted by Tao and Sun has been observed both by computer simulations [16,18,19] and by experiments [3,4,6,7].

In our earlier work [21], we determined the phase diagram of two dipolar systems: (i) colloids without charge (or dipolar hard-spheres) and (ii) colloids with a charge $Ze=300e$ and inverse Debye screening length (in units of the colloid diameter σ) of $\kappa\sigma=10$ (dipolar soft-spheres). The phase diagram of dipolar hard spheres shows fluid, face-centered-cubic (fcc), hexagonal-close-packed (hcp), and bct phases. The phase diagram of dipolar soft spheres shows, in addition to the above mentioned phases, a body-centered-orthorhombic (bco) phase. As we showed, the phase diagram of dipolar soft spheres is in good agreement with the experimental phase diagram in Ref. [3]. We were able to explain the appearance of a body-centered-orthorhombic (bco) phase based on simple arguments. Furthermore, our calculations proposed hexagonal-close-packed (hcp) crystal as the high-density stable phase in systems with dipolar interactions. In this paper, we give a more detailed description of the simulations in Ref. [21]. Also, we discuss the multipole moment expansion method that was used in Ref. [21] to verify the energy difference between the fcc and hcp phases. Finally, we briefly study the structure of the fluid phase.

This paper is organized as follows. In Sec. II we describe the model and the methods used in the simulations. In Sec. III we present the results. In Sec. IV we conclude.

II. MODEL AND METHODS

We use a dipole approximation to describe the pair potential between two dielectric or magnetic particles. Figure 1(a) illustrates the situation and shows two particles with diameter σ that are separated by a vector $\mathbf{r}$. The vector $\mathbf{r}$ forms an angle θ with the z axis, which is parallel to an external electric ($\mathbf{E}$) or magnetic ($\mathbf{H}$) field. In the case of an electric field, the particles and the solvent have a dielectric constant of ϵ_p and ϵ_s, respectively, whereas in the case of a magnetic field, the particles and the solvent have a magnetic susceptibility of

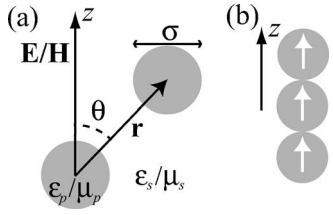

FIG. 1. Dipole-dipole interactions. (a) Two particles with diameter σ connected by a vector $\mathbf{r}$. The vector $\mathbf{r}$ forms an angle θ with the z axis. The external electric ($\mathbf{E}$) or magnetic ($\mathbf{H}$) field is parallel to the z axis. In the case of an electric field, the particles have a dielectric constant ϵ_p and the solvent ϵ_s. In the case of a magnetic field, the particles have a magnetic susceptibility μ_p and the solvent μ_s. (b) The dipole-dipole interaction favors configurations where the dipoles (denoted by the white arrows) are oriented head-to-toe.

μ_p and μ_s, respectively. The external field induces a (electric or magnetic) dipole moment on the particles, which is parallel to the field direction (the z axis). The dipole-dipole interaction is given by

$$\frac{u_{\rm dip}(\mathbf{r})}{k_BT} = \frac{\gamma}{2}\left(\frac{\sigma}{r}\right)^3 (1 - 3\cos^2\theta), \tag{1}$$

where k_B is the Boltzmann constant and T is the temperature. In the case of electric dipoles, the prefactor γ is given by

$$\gamma = \frac{\pi\sigma^3\alpha^2\epsilon_s|\mathbf{E}_{\rm loc}|^2}{8k_BT}, \tag{2}$$

where $\mathbf{E}_{\rm loc}$ is the local electric field, which is a sum of the external field $\mathbf{E}$ and the field induced by the other dipoles $\mathbf{E}_{\rm dip}$ [10,17,22], i.e., $\mathbf{E}_{\rm loc}=\mathbf{E}+\mathbf{E}_{\rm dip}$. In Eq. (2), $\alpha=(\epsilon_p-\epsilon_s)/(\epsilon_p+2\epsilon_s)$ is the polarizability of the particles. In the case of magnetic dipoles, γ is given entirely symmetrically, and it is written as

$$\gamma = \frac{\pi\sigma^3\alpha^2\mu_s|\mathbf{H}_{\rm loc}|^2}{8k_BT}, \tag{3}$$

where $\alpha=(\mu_p-\mu_s)/(\mu_p+2\mu_s)$ and $\mathbf{H}_{\rm loc}=\mathbf{H}+\mathbf{H}_{\rm dip}$ is the local magnetic field [23].

For charged colloids, we supplement the dipole-dipole interaction in Eq. (1) with a soft repulsion caused by like-charge repulsion. According to the Derjaguin-Landau-Verwey-Overbeek (DLVO) theory [24,25], the pair interaction between two charged colloids is given by a repulsive Yukawa (or screened Coulombic) plus the hard core potential as

$$\frac{u_{\rm Y}(r)}{k_BT} = \begin{cases} \epsilon\dfrac{\exp[-\kappa(r-\sigma)]}{r/\sigma}, & r \geqslant \sigma, \\ \infty, & r < \sigma, \end{cases} \tag{4}$$

where

$$\epsilon = \frac{Z^2}{(1+\kappa\sigma/2)^2}\frac{\lambda_B}{\sigma} \tag{5}$$

is a constant prefactor depending on the colloidal charge number Z, the Debye screening length κ^{-1}, and the Bjerrum length $\lambda_B=e^2/\epsilon_s k_BT$ of the solvent. Since we are interested in modeling systems where the Van der Waals attraction is very small due to refractive index matching, we have neglected it in Eq. (4). The phase behavior of repulsive Yukawa particles is well known from earlier studies [26–30], where it has been shown that, depending on the density, prefactor ϵ, and screening length κ^{-1}, the system exhibits fluid, body-centered-cubic (bcc), and face-centered-cubic (fcc) phases.

Using the pair potentials in Eqs. (1) and (4), we perform Monte Carlo (MC) simulations in the canonical ensemble (NVT), where we fix the number of particles N, the volume V, and the temperature T [31]. The simulation box is periodic in all three directions. Typical number of particles in our simulations is $N=144-288$, and cubic, or nearly cubic, simulation boxes are used. Because of the long-range nature of the dipolar interactions, we use the Ewald summation method to evaluate the potential in Eq. (1) [31,32]. Both the Yukawa and the dipolar potential are truncated at half of the shortest box side length. The width of the Gaussian distribution, the tunable parameter in the Ewald sum, is optimized according to the analytical estimates given in Ref. [33].

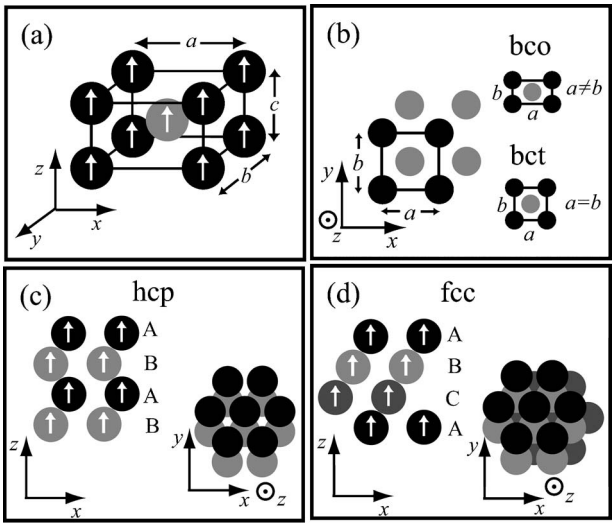

FIG. 2. (a) Body-centered structure in three dimensions, whose conventional unit cell is $a\times b\times c$. The field is along the z axis. The white arrows show the direction of the field-induced dipole moments. The bct structure corresponds to $a=b\neq c$, and the bco to $a\neq b$, $c\neq a$, and $c\neq b$. (b) Top-view of the body-centered structure that can be constructed by placing strings of particles shifted by $c/2$ into two interpenetrating rectangular lattices. (c), (d) The hcp and fcc structures shown in side and top views. The hcp structure has AB stacking of the hexagonal planes; the fcc ABC.

In our simulations, we consider the fluid, bcc, bct, bco, fcc, and hcp phases. The body-centered (bcc, bct, and bco) structures are aligned such that the particles form strings parallel to the z axis (the field direction), see Fig. 2(a). The body-centered box side lengths are given in the x, y, and z axis directions by a, b, and c, respectively. Shown in Fig. 2(b) are the bco and bct structures viewed along the z axis. As can be seen from Fig. 2(b), the bco and bct structures can be constructed by placing strings of particles into two interpenetrating rectangular ($a\times b$) lattices. The particles in the strings are displaced by $c/2$ in the z direction. The bco structure can be thought of as an asymmetric version of the bct structure. The maximum packing of the bct structure is obtained when $a=b=(\sqrt{6}/2)\sigma$ and $c=\sigma$, corresponding to a packing fraction $\eta=\pi\sigma^3N/6V=2\pi/9\approx 0.698$. Note that, the bcc phase has $a=b=c$. The fcc and hcp structures are depicted in Figs. 2(c) and 2(d), respectively. Both fcc and hcp are oriented with the (111) plane perpendicular to the z axis.

The phase behavior was studied by MC simulation runs and by Helmholtz free energy calculations. We used the MC simulation runs to obtain a rough estimate of the phase behavior, after which the more accurate free energy calculations were performed to check the result and to determine the phase boundaries more exactly. Phase coexistence regions were determined by a common tangent construction from Helmholtz free energies that were calculated using thermodynamic integration methods. We used the λ-integration method for the fluid phase and the Frenkel-Ladd method for

the solid phase [31,34]. As a reference state, we used the hard-sphere fluid for the fluid phase and the noninteracting Einstein crystal for the solid phase. The numerical integration was done with a Gaussian quadrature using 10 (or in some cases 20) integration points. The statistical averages needed in the free energy calculations were calculated from MC simulation runs that consisted of 10 000–200 000 MC steps (trial moves per particle), and that were first equilibrated with the same (or similar) number of MC steps.

Due to the dipole-dipole interaction, compression along the z axis lowers the energy of all our crystal phases. Therefore, in order to get reliable results, we need to optimize the z axis side length. For the bct, fcc, and hcp phases, we calculated the free energies for various z axis side lengths and used the minimum value to determine the phase boundaries. In the case of soft repulsions, the bco unit box symmetry, given by c and the ratio a/b, was determined by varying a/b and c to find the minimum of the Madelung energy (energy of an ideal crystal per particle). If the minimum state had strings in touching configurations ($c=\sigma$), we set $c=1.01\sigma$ to ensure that efficient MC sampling of the system is still possible. For some systems, also other choices such as $c=1.04\sigma$ and $c=1.005\sigma$ were tried, but in general, the results did not depend strongly on the choice of c.

III. RESULTS

A. Phase diagrams

Our model presented in Sec. II can be described by four independent dimensionless parameters: the packing fraction η, the strength of the dipolar interaction γ, the colloidal charge Z, and the inverse screening length $\kappa\sigma$. We fix the colloidal charge Z and study the phase behavior in a constant $\kappa\sigma$ plane, i.e., our phase diagrams are plotted in the (γ, η) representation.

In Fig. 3, we show the phase diagram of the dipolar hard spheres (i.e., $\epsilon=0$) in the (γ, η) representation. At zero dipole moment strength ($\gamma=0$), the well-known hard-sphere fluid-fcc coexistence with the coexisting phases at $\eta_{\text{fluid}}=0.494$ and at $\eta_{\text{fcc}}=0.545$ is recovered. At $\gamma>0$, the fluid-fcc coexistence switches to fluid-hcp coexistence. Increasing the dipole moment strength from $\gamma=0$ to $\gamma=6.5$ does not change the fluid-hcp coexistence much. At $\gamma>6.5$, the bct phase is the stable crystalline phase at low densities, while the hcp phase is, due to more efficient packing, still the stable phase at packing fractions $\eta\gtrsim 0.57$. At the dipole moment strength $\gamma\approx 8.0$, the system phase separates into a (string) fluid phase and a bct phase. Figure 4(a) shows a snapshot of the string fluid phase, where the view is along the z axis (i.e., parallel with the field) and we observe strings that look similar to individual particles or small clusters of particles. The strings can be seen in the inset of Fig. 4(a), which shows the same snapshot but viewed such that the z axis is horizontal. The statepoint of the snapshot in Fig. 4(a), and the other snapshots in Fig. 4, are denoted by the letters (a), (b), (c), and (d) in Fig. 3. The fluid-bct phase coexistence region broadens with increasing dipole moment strength and at $\gamma=13.1$, the fluid phase has turned into a very low density gas phase (or void). Figure 4(b) shows a snapshot of an MC simulation well inside the gas-bct phase coexistence region at ($\gamma=13.1$, $\eta=0.4$). For comparison, a snapshot of a stable bct phase with the same γ is shown in Fig. 4(c).

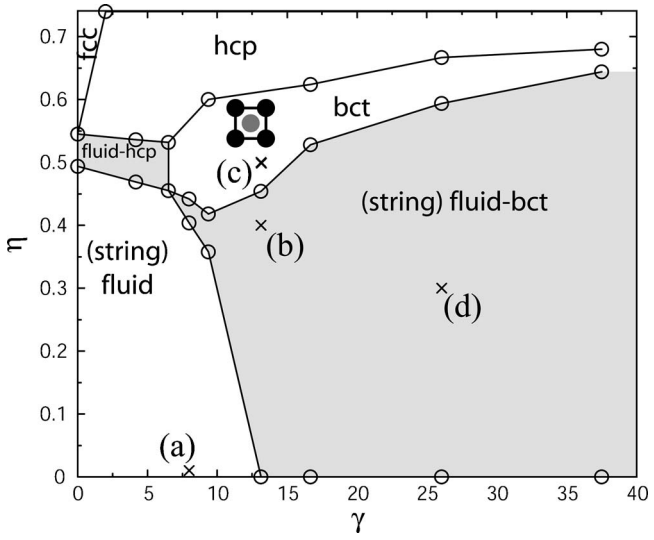

FIG. 3. The phase diagram of dipolar hard-sphere particles in the (dipole moment strength γ, packing fraction η) representation. The circles denote points where the phase boundary was determined and the grey areas denote coexistence regions (where tie lines are vertical). The letters (a), (b), (c), and (d) mark the state points where the snapshots shown in Fig. 4 are taken.

At $\gamma>13.1$, the gas-bct coexistence broadens further and, at $\gamma\approx 38$, the bct phase has packing fraction $\eta_{\text{bct}}=0.66$ close

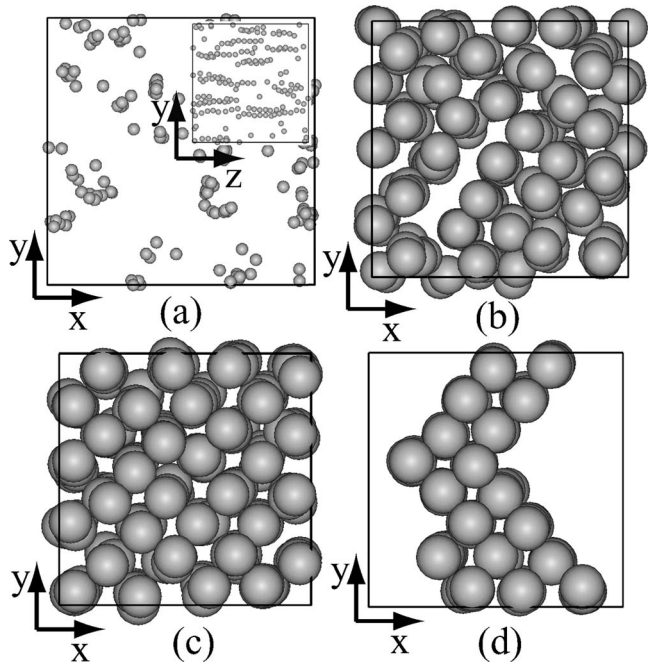

FIG. 4. Snapshots of the dipolar hard-sphere systems in (a) string fluid phase at ($\gamma=8.0$, $\eta=0.01$), (b) gas-bct coexistence phase at ($\gamma=13.1$, $\eta=0.4$), (c) stable bct phase at ($\gamma=13.1$, $\eta=0.5$), and (d) gas-bct coexistence phase at ($\gamma=26.1$, $\eta=0.3$). See Fig. 3 for the locations of the snapshots in the phase diagram.

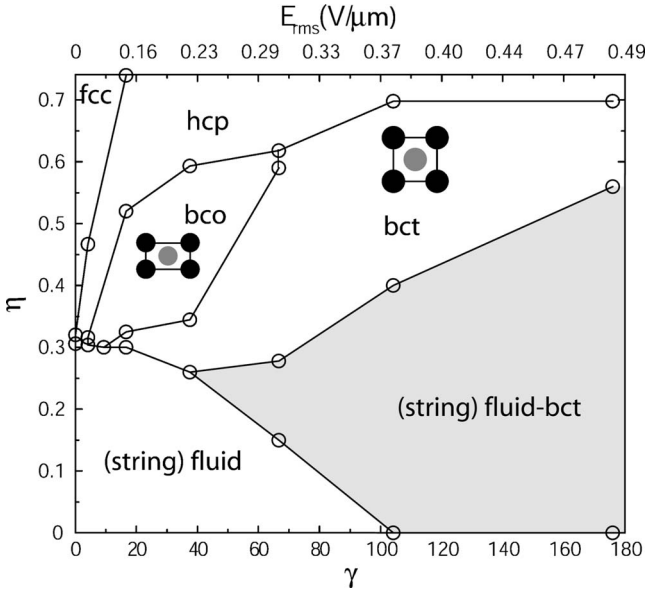

FIG. 5. The phase diagram of dipolar soft sphere particles with Yukawa parameters $\kappa\sigma=10.0$ and $Z=300$ (that with $\lambda_B/\sigma=0.005$ correspond to a contact value $\epsilon=12.54$) in the (dipole moment strength γ, packing fraction η) representation. The circles denote points where the phase boundary was determined and the grey area denotes the coexistence region (where tie lines are vertical). The upper horizontal axis gives an estimate of the root-mean-square external electric field, see text for details.

to the maximum packing. Snapshot Fig. 4(d) illustrates the gas-bct phase separation at high dipole moment strength ($\gamma=26.1$). We expect at higher dipole moment strengths (i.e., $\gamma>38$), a very broad gas-bct coexistence between a void (low density gas phase) with packing fraction $\eta\approx 0.0$ and a bct phase at the maximum packing $\eta=0.698$. As can be seen from Fig. 3, the stability of the hcp phase is reduced when the dipole moment strength is increased, and beyond $\gamma\approx 25$ the hcp phase is stable only above the maximum bct packing.

The ground-state ($\gamma=\infty$) phase behavior of dipolar hard spheres has been studied in Ref. [20], where the authors found a gas-bct coexistence at $\eta\in[0,0.698]$, a stable high-density bco phase at $\eta\in[0.698,0.724]$, a bco-hcp coexistence at $\eta\in[0.698,0.740]$, and a stable hcp phase at $\eta=0.740$. This sequence of phases and in particular, the presence of the bco phase, should also be present in our dipolar hard sphere phase diagram at $\gamma\gg 40$, but we did not extend our simulations to high enough γ to observe it. The reason for this is that at very high values of γ, the simulations are hampered by sampling problems as the displacement moves become difficult due to strong dipole-dipole interactions. Note that for dipolar soft spheres (which are discussed next) it is possible to reach higher γ because the soft repulsion compensates partly for the dipolar interaction.

Next, we consider the case where the particles, in addition to the dipole-dipole interaction, interact via the Yukawa repulsion in Eq. (4) with parameters $\kappa\sigma=10.0$ and $Z=300$. For a solvent with Bjerrum length $\lambda_B/\sigma=0.005$, these parameters correspond to a contact value $\epsilon=12.54$. The phase diagram for this dipolar soft sphere system is shown in Fig. 5. At zero

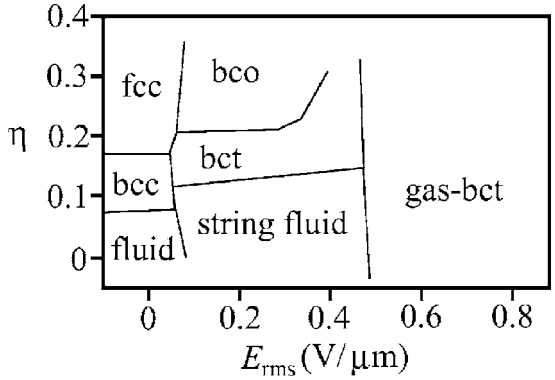

FIG. 6. A reproduction of the experimental phase diagram in Ref. [3].

electric field, the phase diagram in Fig. 5 shows a fluid-fcc phase coexistence with the two phases at packing fractions $\eta_{\text{fluid}}=0.31$ and $\eta_{\text{fcc}}=0.32$. At $\gamma>0$, the fcc phase is replaced by the hcp phase. As is seen from Fig. 5, even a small amount of electric field ($\gamma\gtrsim 4$) is sufficient to suppress the stability region of the hcp phase considerably and to replace it by a bco phase, which is stable at low densities for $4\leqslant\gamma\leqslant 10$. In the phase diagram in Fig. 5, at $\gamma\approx 17$, the bct phase emerges as the stable low-density crystal. Further increase of the dipole moment strength from $\gamma\approx 17$ reduces the significance of the soft repulsion relative to the dipolar attraction, therefore increasing the region of the stable bct phase. Finally, at $\gamma\approx 67$, the bco phase vanishes completely. Increasing the dipole moment strength reduces the stability region of the hcp phase and, at $\gamma\gtrsim 100$, the hcp phase is only stable at packing fractions higher than the maximum body-centered packing.

The phase diagram in Fig. 5 shows that the fluid-bct coexistence region, starting at $\gamma\approx 38$, broadens quickly with increasing dipole moment strength γ. At $\gamma\approx 67$, the fluid phase in coexistence with the bct phase consists of strings of particles (string fluid phase), while the fluid phase is extremely dilute, i.e., $\eta\approx 0$, for $\gamma\gtrsim 100$. At $\gamma>180$, we expect that the coexisting bct phase reaches the maximum packing $\eta\approx 0.698$.

In Fig. 6, we plot a reproduction of the experimental phase diagram of Ref. [3]. We have renamed some of the phases in the experimental phase diagram. Firstly, we call the space-filling tetragonal (sft) phase of Ref. [3] bct. Secondly, the non-space-filling bct phase of Ref. [3], which consist of small bct crystallites with voids, corresponds to our gas-bct coexistence. Experimentally, one observes a micro phase separation instead of a macroscopic phase separation, which depends strongly on the kinetics and dynamics of the phase separation and on how fast the electric field is switched on. For comparison with Fig. 6, the upper horizontal axis in Fig. 5 gives the (root mean square) electric field strength $E_{\text{r.m.s.}}$. The γ to $E_{\text{r.m.s.}}$ conversion is done using

$$E_{\text{r.m.s.}}=2\frac{\left|1-\alpha\frac{\pi}{6}\right|}{|\alpha|}\sqrt{\frac{k_BT\gamma}{\epsilon_s\sigma^3\pi}}, \tag{6}$$

where we used parameter values that correspond to the experimental system of Ref. [3]: $\alpha=-0.105$, $T=300$ K, ϵ_s

=5.6, and $\sigma=2$ μm. For the derivation of Eq. (6), see, e.g., Refs. [10,17,22]. We have assumed a cubic lattice, for which the local field is given by $\mathbf{E}_{\mathrm{loc}}=\mathbf{E}/(1-\alpha\pi/6)$ [10]. As can be checked from Figs. 5 and 6, the external electric field strength $E_{\mathrm{r.m.s.}}$ has the same order of magnitude in both phase diagrams. Our phase diagram for dipolar soft spheres in Fig. 5 shows a remarkable structural agreement with the experimental phase diagram in Fig. 6. Both phase diagrams show, at low electric field strength, the same sequence of fluid, bct, and bco phases upon increasing η, and at high electric fields, phase separation between a gas (void) and a bct phase. The main difference between the two phase diagrams is the bcc phase, which is seen experimentally at zero electric field but which is not present in the theoretical phase diagram. This dissimilarity is due to the different Z and κ in the experiments and the simulations. More exact determination of these parameters would require further characterization of the experimental conditions.

B. Stability of bco phase

In this section, we explain how the soft repulsion give rise to the bco phase. Note that, we mean the bco phase in the phase diagram in Fig. 5, not the high-density bco phase discussed earlier, which, according to Ref. [20], appears at very high γ in the dipolar hard sphere phase diagram in Fig. 3.

The emergence of the bco phase is most easily explained as follows. Due to dipolar interactions, the particles form strings in the z direction. If two strings are close to each other, it is favorable to shift one string by $c/2$ in the z direction with respect to the other string, as the dipole-dipole interaction favors configurations with small angles θ, see Eq. (1). Consequently, two kind of strings, say A and B, are obtained. In Fig. 2(b), A strings are black and B strings are grey. The interactions between the strings are such that similar strings (A-A and B-B) repel each other more than dissimilar strings (A-B). This is why the bct is stable: it minimizes the A-B distance. Soft Yukawa repulsion of A-A strings and A-B strings are very similar (A-B being slightly weaker), and it favors configurations where all neighboring strings have almost equal distances. This is achieved by increasing the ratio a/b. Hence, the bco phase. Note that in a hexagonal state (which is the ground state if all strings are similar) all nearest neighbors distances are equal and $a/b=\sqrt{3}\approx 1.73$.

In order to make the above description more quantitative, we calculated the Madelung energies for a bco crystal at a fixed η as a function of a/b. Figure 7 shows the change in Madelung energy

$$\Delta U_M(a/b) = U_M(a/b) - U_M(1) \tag{7}$$

of a bco crystal (with $c=\sigma$) at packing fractions $\eta=0.27$, 0.4, and 0.5. At $\eta=0.27$, the minimum of the Madelung energy is at $a/b=1$ and, therefore, the ground state is bct. At $\eta=0.4$ and 0.5, the minimum is at $a/b\approx 1.4$, meaning that the ground state is bco. Next, we split the Madelung energy into Yukawa and dipolar parts as

$$\Delta U_M(a/b) = \Delta U_M^Y(a/b) + \Delta U_M^{\mathrm{dip}}(a/b). \tag{8}$$

Figure 8 shows the Yukawa $[\Delta U_M^Y(a/b)]$ part of the Madelung energy and the inset the dipolar part $[\Delta U_M^{\mathrm{dip}}(a/b)]$. As

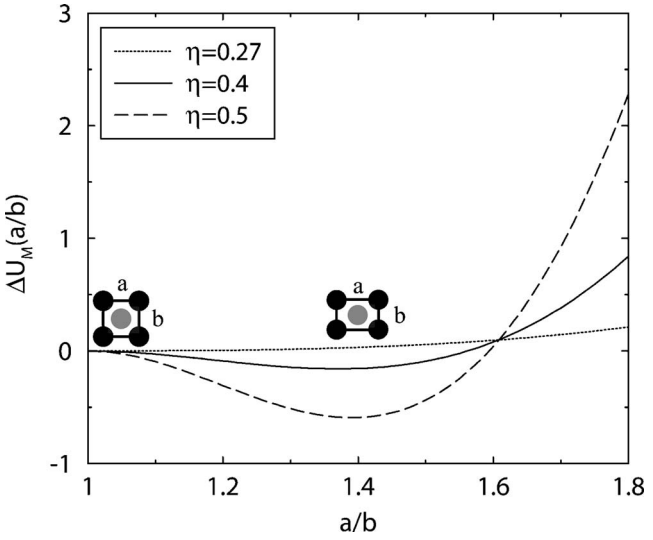

FIG. 7. The change in the Madelung energy [see Eq. (7)] of bco crystals as a function of the asymmetry parameter a/b for dipolar soft spheres with $\kappa\sigma=10.0$, $Z=300$ (corresponding to $\epsilon=12.54$ with $\lambda_B/\sigma=0.005$) and $\gamma=37.5$. The dotted line shows the result for packing fraction $\eta=0.27$, the full line for $\eta=0.4$, and the dashed line for $\eta=0.5$.

can be seen from Fig. 8, the dipolar part $\Delta U_M^{\mathrm{dip}}(a/b)$, increases monotonically with a/b, while $\Delta U_M^Y(a/b)$ has a minimum at $a/b>1.5$. Thus, the bco phase is stabilized by soft repulsion.

C. Multipole moment expansion

The reason why the hcp phase is more stable than the fcc phase is due to the difference between the Madelung energies of the two structures: The hcp structure with the orientation

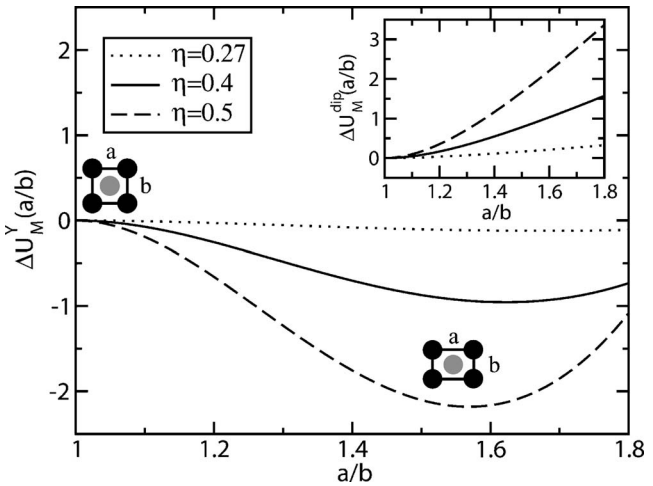

FIG. 8. Yukawa (or the soft repulsion) part of the change in the Madelung energy of bco crystals as a function of the asymmetry parameter a/b. The dotted line shows the result for packing fraction $\eta=0.27$, the full line for $\eta=0.4$, and the dashed line for $\eta=0.5$. In order to enable a comparison, the results have been shifted by $w_Y(1)$ to have the same value at $a/b=1$. The inset shows the dipolar part of the Madelung energy.

shown in Fig. 2(c) has a Madelung energy $U_M(\text{hcp}) = -0.37066 \times 4\gamma$ (as in Refs. [7,17]), while the fcc structure (whose energy is independent of the orientation) has a Madelung energy $U_M(\text{fcc}) = -0.37024 \times 4\gamma$ (as in Refs. [10,17]). Although the Madelung energy difference between hcp and fcc is small, $1.7\gamma \times 10^{-3} k_B T$ per particle, so is their zero-field free energy difference: For hard spheres [35], the free energy per particle of the fcc is about $1 \times 10^{-3} k_B T$ lower than that of the hcp. Therefore, for dipolar hard spheres, the hcp is expected to be stable for $\gamma \gtrsim 1$, which is consistent with Fig. 3.

In order to check that the Madelung energy difference between the fcc and hcp crystals is a real effect and not an artifact of the dipole approximation, we calculated the difference using the multipole moment expansion method of Ref. [36]. The total Coulomb energy per particle is given by

$$u = -\frac{2\pi a^3}{3\eta k_B T} |\mathbf{E}|^2 \epsilon_{\text{eff}}, \tag{9}$$

where $a = \sigma/2$ is the radius of the particles constituting the structure, η is the volume fraction, and $\mathbf{E}$ is the applied electric field. The method in Ref. [36] allows one to calculate the effective dielectric constant ϵ_{eff} with any number of multipoles. In the following we briefly describe the method. For more details we refer the reader to the original article [36]. We consider $\tau_{\max}+1$ spheres with a dielectric constant ϵ_p in one unit cell embedded in a solvent with a dielectric constant ϵ_s. According to Ref. [36], The effective dielectric constant ϵ_{eff} is given by

$$\epsilon_{\text{eff}} = \epsilon_s [1 - F(s)], \tag{10}$$

where

$$F(s) = \frac{\eta}{\tau_{\max}+1} \sum_{u=1}^{u_{\max}} \frac{\left| \sum_{\tau=0}^{\tau_{\max}} U_{u,\tau 10} \right|^2}{s - s_u}. \tag{11}$$

In Eq. (11), $U_{u,\tau 10}$ is the (τ, $l=1$, $m=0$) component of the uth eigenvector of matrix $\Gamma = \{\Gamma_{\tau lm,\tau' l' m'}\}$, s_u is the corresponding eigenvalue, $s = 1/(1-\epsilon_p/\epsilon_s)$ is a material parameter, and τ is the index of the sphere in the unit cell. Note that $\tau_{\max}=1$ for hcp and $\tau_{\max}=0$ for Bravais lattices such as fcc and bct. The index $m = \{-l, \ldots, l\}$ and $l = \{1, \ldots, l_{\max}\}$. The elements of the matrix Γ are defined as

$$\Gamma_{\tau lm,\tau' l' m'} = \sum_{\tau=0}^{\tau_{\max}} \sum_{\mathbf{R}} \hat{\Gamma}_{lm,l' m'}(\mathbf{R} + \mathbf{R}_\tau), \tag{12}$$

where the summation goes over all lattice points $\mathbf{R}$, $\mathbf{R}_\tau$ is the displacement of the τth sphere with respect to the origin, and

$$\hat{\Gamma}_{lm,l' m'}(\mathbf{R}) = s_{l'} \int d\mathbf{r}^3 \xi(\mathbf{r}) \nabla \phi^*_{lm}(\mathbf{r}) \cdot \nabla \phi_{l' m'}(\mathbf{r} + \mathbf{R}). \tag{13}$$

In Eq. (13), $\xi(\mathbf{r})$ is the characteristic function of the particles, having value 1 inside the sphere and 0 outside, ϕ^*_{lm} denotes the complex conjugate of ϕ_{lm}, and

$$\phi_{lm}(\mathbf{r}) = f_l(r) Y_l^m(\theta, \phi), \tag{14}$$

$$f_l(r) = \begin{cases} \dfrac{(r/a)^l}{\sqrt{la}}, & \text{for } r < a, \\ \dfrac{1}{(r/a)^{l+1}\sqrt{la}}, & \text{for } r > a, \end{cases} \tag{15}$$

where $Y_l^m(\theta, \phi)$ are the spherical harmonics and the spherical coordinate system is defined as [37]

$$\begin{aligned} r_x &= r \cos(\phi)\sin(\theta), \\ r_y &= r \sin(\phi)\sin(\theta), \\ r_z &= r \cos(\theta), \end{aligned} \tag{16}$$

where $\theta \in [0, \pi]$ and $\phi \in [0, 2\pi)$. We define the relationship between the spherical harmonics and the associated Legendre polynomials as

$$Y_l^m(\theta, \phi) = \sqrt{\frac{2l+1}{4\pi} \frac{(l-m)!}{(l+m)!}} P_l^m(\cos\theta) e^{im\phi}, \tag{17}$$

where the Condon-Shortley phase $(-1)^m$ is included in the Legendre polynomials (unlike in Ref. [36]). After evaluating the integrals in Eq. (13), we obtain

$$\hat{\Gamma}_{lm,l' m'}(0) = \frac{l}{2l+1} \delta_{ll'} \delta_{mm'},$$

$$\hat{\Gamma}_{lm,l' m'}(\mathbf{R}) = \sqrt{\frac{ll'}{(2l+1)(2l'+1)}} B_{lm,l' m'} S(\mathbf{R}), \tag{18}$$

where

$$B_{lm,l' m'} = (-1)^{l'+m} \sqrt{4\pi} \sqrt{\frac{(l+l'+m'-m)!(l+l'+m-m')!}{(2l+2l'+1)(l+m)!(l-m)!(l'+m')!(l'-m')!}}, \tag{19}$$

and

$$S(\mathbf{R}) = \frac{Y_{l+l'}^{m'-m}(\theta, \phi)}{R^{l+l'+1}}. \tag{20}$$

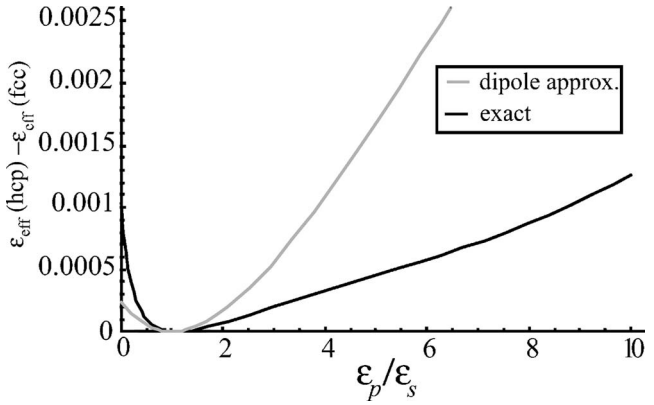

FIG. 9. The difference in the effective dielectric constants of the hcp and fcc crystals at packing fraction $\eta \approx 0.72948$ as a function of the ratio ϵ_p/ϵ_s. The grey and black lines are the results of the dipole approximation and the exact calculation, respectively.

In Eq. (18), $\delta_{ll'}$ and $\delta_{mm'}$ are discrete Kronecker delta functions. As noted in Ref. [36], the summation in Eq. (12) is only conditionally convergent for $l+l' \leqslant 2$ as it involves terms which decay slower than $1/R^3$. Therefore, we used the Ewald method to evaluate the sums with $l+l' \leqslant 4$ (Note that in Ref. [36], the Ewald method was used for $l+l' \leqslant 6$.) The Ewald sums are given in the Appendix. Once the matrix elements $\Gamma_{\tau lm,\tau' l' m'}$ are determined from Eq. (12), the eigenvectors U_u and the eigenvalues s_u can be solved easily. The calculation was implemented with MATHEMATICA®. We tested our program by calculating the dielectric constants for the bct, fcc, hcp, and bcc crystals, and compared the results with the numerical values given in Ref. [36]. In order to obtain the same accuracy as in Ref. [36], 20–27 multipole contributions (i.e., $l_{\max}=20-27$) were included in the calculation.

In Fig. 9, we plot the difference between the effective dielectric constants of the hcp and fcc crystals at packing fraction $\eta \approx 0.72948$ as a function of the ratio ϵ_p/ϵ_s. The grey line plots the result of the dipole approximation where $l_{\max}=1$, and the black lines plots the result of the exact calculation where $l_{\max}=27$. As can be seen from Fig. 9, the hcp crystal has a higher effective dielectric constant than the fcc crystal for $\epsilon_p/\epsilon_s > 0$, which results, according to Eq. (9), in a lower energy than fcc. Figure 9 also shows that in the region where $\epsilon_p/\epsilon_s < 1$, the contribution from the multipole moments favors the hcp phase even more than what is expected based on the dipole approximation alone. Note that the experiments in Ref. [3] are in this region as they have $\epsilon_p/\epsilon_s \approx 0.7$. In the region where $\epsilon_p/\epsilon_s > 1$, the multipole moments decrease the energy difference between hcp and fcc crystals.

D. Fluid phase

In both hard and soft dipolar systems, we observed a highly inhomogeneous fluid phase: The MC simulations showed large local density fluctuations in the fluid phase, reminiscent of a gas-liquid phase separation. However, no spinodal instability was found. An example of a Helmholtz free energy (F) curve is shown in Fig. 10, where we plot

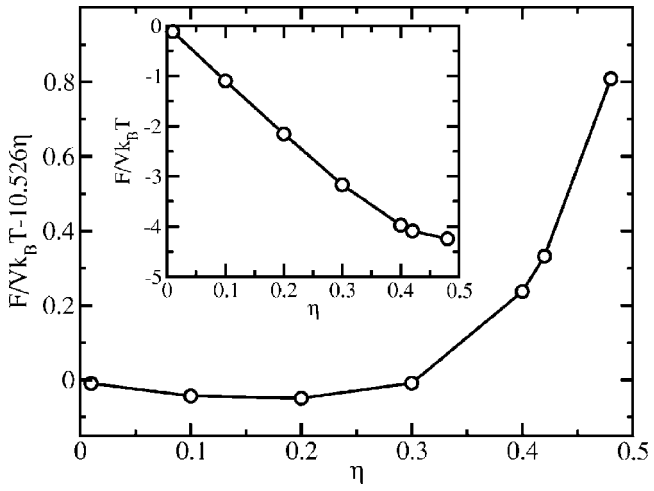

FIG. 10. The Helmholtz free energy per volume F/Vk_BT as a function of η for dipolar hard sphere fluid with $\gamma=8.0$. In the main figure, a linear fit to the first four data points has been subtracted. The inset shows the original free energy data. The lines are guide to the eye.

F/V as a function of η for the dipolar hard sphere fluid at dipole moment strength $\gamma=8.0$. This system has an inhomogeneous fluid phase at $\eta \leqslant 0.3$, as can be seen from Fig. 4(a) that shows a snapshot of the system at $\eta=0.01$. However, as Fig. 10 shows, the free energy density curve is convex, and therefore, no gas-liquid phase separation is possible. On the other hand, the free energy density F/V is almost linear with η. This means that the compressibility, which is proportional to the second derivative of F/V with respect to η, is very small. The small compressibility explains the appearance of an inhomogeneous fluid phase.

IV. CONCLUSIONS

We have determined the phase diagrams of dipolar hard and soft spheres using Monte Carlo simulations. Two systems were considered: (i) colloids without charge (or dipolar hard spheres) and (ii) colloids with charge $Ze=300e$ and inverse Debye screening length of $\kappa\sigma=10$ (dipolar soft spheres). The simulations correspond to dielectric (or magnetic) particles in an external electric (or magnetic) field. The phase diagrams were plotted as a function of the dipole moment strength γ and the packing fraction η. In the phase diagram of dipolar hard spheres, we found stable regions of (string-) fluid, fcc, hcp, and bct phases, and regions of fluid-hcp and fluid-bct coexistence. In the phase diagram of soft spheres, we found all the above phases and also a stable region of the asymmetric bco phase. The stability of the bco phase was explained based on simple Madelung energy considerations. We found the hcp phase as the new stable phase in the high packing fraction region. In this region, the hcp phase is more stable than the fcc phase, because of its lower Madelung energy, and more stable than the bct phase, because of its higher entropy. We showed that the hcp phase has a lower Madelung energy than the fcc phase even when one goes beyond the dipole approximation and performs the

full calculation which includes all multipole moments. Our results show that bulk hcp, bct, and bco crystals, can be stabilized and therefore realized experimentally by applying an external electric or magnetic field. It is important to remember that these crystal phases are unstable in the absence of a field. Finally, in both systems, we observed an inhomogeneous fluid phase. However, we did not find any evidence for a gas-liquid phase instability. Our free energy calculations showed that the free energy density vs packing fraction is close to linear, indicating a small compressibility, which explains why the fluid phase appears inhomogeneous.

TABLE I. The relation between the tensors (A4)–(A6) and the terms in the sum in Eq. (A1). Here $L=l+l'$ and $M=m'-m$.

L	M	$\frac{1}{\lvert\mathbf{R}+\mathbf{r}\rvert^{L+1}}Y_L^M(\theta,\phi)$
2	2	$\sqrt{\frac{5}{96\pi}}(T^2_{xx}-T^2_{yy}+2\mathrm{i}T^2_{xy})$
2	1	$-\sqrt{\frac{5}{24\pi}}(T^2_{xz}+\mathrm{i}T^2_{yz})$
2	0	$\frac{1}{2}\sqrt{\frac{5}{4\pi}}T^2_{zz}$
3	3	$\frac{1}{120}\sqrt{\frac{35}{\pi}}[T^3_{xxx}-3T^3_{xyy}+\mathrm{i}(3T^3_{xxy}-T^3_{yyy})]$
3	2	$\frac{1}{60}\sqrt{\frac{105}{2\pi}}(T^3_{yyz}-T^3_{xxz}-2\mathrm{i}T^3_{xyz})$
3	1	$\frac{1}{24}\sqrt{\frac{21}{\pi}}(T^3_{zzx}+\mathrm{i}T^3_{zzy})$
3	0	$-\frac{1}{12}\sqrt{\frac{7}{\pi}}T^3_{zzz}$
4	4	$\frac{1}{16\sqrt{70\pi}}[T^4_{xxxx}-6T^4_{xxyy}+T^4_{yyyy}+4\mathrm{i}(T^4_{xxxy}-T^4_{xyyy})]$
4	3	$-\frac{1}{8\sqrt{35\pi}}[T^4_{xxxz}-3T^4_{xyyz}+\mathrm{i}(3T^4_{xxyz}-T^4_{yyyz})]$
4	2	$\frac{1}{8\sqrt{10\pi}}(T^4_{xxzz}-T^4_{yyzz}+2\mathrm{i}T^4_{xyzz})$
4	1	$-\frac{1}{8\sqrt{5\pi}}(T^4_{zzzx}+\mathrm{i}T^4_{zzzy})$
4	0	$\frac{1}{16\sqrt{\pi}}T^4_{zzzz}$

ACKNOWLEDGMENTS

We thank A. van Blaaderen and J. H. J. Thijssen for helpful comments and critical reading of the manuscript, and A. Yethiraj and R. van Roij for fruitful conversations. This work is part of the research program of the "Stichting voor Fundamenteel Onderzoek der Materie (FOM)," which is financially supported by the "Nederlandse Organisatie voor Wetenschappelijk Onderzoek (NWO)." We thank the Dutch National Computer Facilities foundation for access to the SGI Origin3800. The High Performance Computing group of Utrecht University is gratefully acknowledged for ample computer time.

APPENDIX: EWALD SUMS

In this appendix, we essentially repeat the Appendix D of Ref. [36]. This is done partly because the original article contains some typos. Essentially, the summations in Eq. (12) are of the form

$$\sum_{\mathbf{R}}\frac{Y_L^M(\theta,\phi)}{\lvert\mathbf{R}+\mathbf{r}\rvert^{L+1}}, \tag{A1}$$

where $L=l+l'$ and $M=m'-m$. As noted in Ref. [36], the summation in Eq. (A1) can be related to summations over the following tensors, which are obtained by successive differentiations with respect to $\mathbf{r}$

$$T^0=\frac{1}{\lvert\mathbf{R}+\mathbf{r}\rvert}, \tag{A2}$$

$$T^1_i=-\frac{(\mathbf{R}+\mathbf{r})_i}{\lvert\mathbf{R}+\mathbf{r}\rvert^3}, \tag{A3}$$

$$T^2_{ij}=\frac{3(\mathbf{R}+\mathbf{r})_i(\mathbf{R}+\mathbf{r})_j}{\lvert\mathbf{R}+\mathbf{r}\rvert^5}-\frac{\delta_{ij}}{\lvert\mathbf{R}+\mathbf{r}\rvert^3}, \tag{A4}$$

$$T^3_{ijk}=-\frac{15(\mathbf{R}+\mathbf{r})_i(\mathbf{R}+\mathbf{r})_j(\mathbf{R}+\mathbf{r})_k}{\lvert\mathbf{R}+\mathbf{r}\rvert^7}+\frac{3}{\lvert\mathbf{R}+\mathbf{r}\rvert^5}[\delta_{ij}(\mathbf{R}+\mathbf{r})_k+\delta_{ik}(\mathbf{R}+\mathbf{r})_j+\delta_{jk}(\mathbf{R}+\mathbf{r})_i], \tag{A5}$$

and

$$T^4_{ijkn}=\frac{105(\mathbf{R}+\mathbf{r})_i(\mathbf{R}+\mathbf{r})_j(\mathbf{R}+\mathbf{r})_k(\mathbf{R}+\mathbf{r})_n}{\lvert\mathbf{R}+\mathbf{r}\rvert^9}-\frac{15}{\lvert\mathbf{R}+\mathbf{r}\rvert^7}[\delta_{in}(\mathbf{R}+\mathbf{r})_j(\mathbf{R}+\mathbf{r})_k+\delta_{jn}(\mathbf{R}+\mathbf{r})_i(\mathbf{R}+\mathbf{r})_k+\delta_{kn}(\mathbf{R}+\mathbf{r})_i(\mathbf{R}+\mathbf{r})_j]-\frac{15(\mathbf{R}+\mathbf{r})_n}{\lvert\mathbf{R}+\mathbf{r}\rvert^7}[\delta_{ij}(\mathbf{R}+\mathbf{r})_k+\delta_{ik}(\mathbf{R}+\mathbf{r})_j+\delta_{jk}(\mathbf{R}+\mathbf{r})_i]$$

$$+\frac{3}{|\mathbf{R}+\mathbf{r}|^5}[\delta_{ij}\delta_{kn}+\delta_{ik}\delta_{jn}+\delta_{jk}\delta_{in}], \tag{A6}$$

where $(\mathbf{R}+\mathbf{r})_i$ is the ith $(=\{x,y,z\})$ component of the vector $\mathbf{R}+\mathbf{r}$. The relation between the tensors in Eqs. (A4)–(A6) with the terms $Y_L^M(\theta,\phi)/|\mathbf{R}+\mathbf{r}|^{L+1}$ in the sum (A1) are given in Table I. Note that, as $L=l+l'\geqslant 2$, we do not list terms with $L<2$. Thus, Table I can be used to convert the sums in Eq. (A1) to sums over the tensors. The advantage of this is that the tensor sums can be evaluated using the Ewald summation as shown in the following. The zeroth order tensor sum is given by

$$\tilde{T}^0=\sum_{\mathbf{R}}T^0=\sum_{\mathbf{R}}\frac{\mathrm{erfc}(\beta|\mathbf{R}+\mathbf{r}|)}{|\mathbf{R}+\mathbf{r}|}+\sum_{\mathbf{G}}\frac{4\pi}{vG^2}\exp(-G^2/4\beta^2)\times\exp(-\mathrm{i}\mathbf{G}\cdot\mathbf{r}), \tag{A7}$$

where $\mathbf{G}$ is the reciprocal vector of $\mathbf{R}$, v is the unit cell volume, and β is a free parameter that is chosen to optimize convergence. Separating out the divergent part of Eq. (A7) and taking successive derivatives with respect to $\mathbf{r}_i$, we obtain

$$\tilde{T}^2_{ij}=-\sum_{\mathbf{G}\neq 0}\frac{4\pi}{vG^2}G_iG_j\exp(-G^2/4\beta^2)\exp(-\mathrm{i}\mathbf{G}\cdot\mathbf{r})+\sum_{\mathbf{R}}\left[\mathrm{erfc}(\beta|\mathbf{R}+\mathbf{r}|)+\left(\frac{4\beta^3|\mathbf{R}+\mathbf{r}|^3}{3\sqrt{\pi}}+\frac{2\beta|\mathbf{R}+\mathbf{r}|}{\sqrt{\pi}}\right)\exp(-\beta^2|\mathbf{R}+\mathbf{r}|^2)\right]T^2_{ij}$$
$$+\sum_{\mathbf{R}}\frac{4\beta^3}{3\sqrt{\pi}}\delta_{ij}\exp(-\beta^2|\mathbf{R}+\mathbf{r}|^2), \tag{A8}$$

$$\tilde{T}^3_{ijk}=\mathrm{i}\sum_{\mathbf{G}\neq 0}\frac{4\pi}{vG^2}G_iG_jG_k\exp(-G^2/4\beta^2)\exp(-\mathrm{i}\mathbf{G}\cdot\mathbf{r})+\sum_{\mathbf{R}}\left[\mathrm{erfc}(\beta|\mathbf{R}+\mathbf{r}|)+\left(\frac{4\beta^3|\mathbf{R}+\mathbf{r}|^3}{3\sqrt{\pi}}+\frac{2\beta|\mathbf{R}+\mathbf{r}|}{\sqrt{\pi}}\right)\exp(-\beta^2|\mathbf{R}+\mathbf{r}|^2)\right]T^3_{ijk}$$
$$-\sum_{\mathbf{R}}\frac{8\beta^5}{\sqrt{\pi}}\frac{(\mathbf{R}+\mathbf{r})_i(\mathbf{R}+\mathbf{r})_j(\mathbf{R}+\mathbf{r})_k}{|\mathbf{R}+\mathbf{r}|^2}\exp(-\beta^2|\mathbf{R}+\mathbf{r}|^2), \tag{A9}$$

and

$$\tilde{T}^4_{ijkn}=\sum_{\mathbf{G}\neq 0}\frac{4\pi}{vG^2}G_iG_jG_kG_n\exp(-G^2/4\beta^2)\exp(-\mathrm{i}\mathbf{G}\cdot\mathbf{r})+\sum_{\mathbf{R}}\left[\mathrm{erfc}(\beta|\mathbf{R}+\mathbf{r}|)+\left(\frac{4\beta^3|\mathbf{R}+\mathbf{r}|^3}{3\sqrt{\pi}}+\frac{2\beta|\mathbf{R}+\mathbf{r}|}{\sqrt{\pi}}\right)\right.$$
$$\left.\times\exp(-\beta^2|\mathbf{R}+\mathbf{r}|^2)\right]T^4_{ijkn}-\sum_{\mathbf{R}}\frac{8\beta^5}{3\sqrt{\pi}}(\mathbf{R}+\mathbf{r})_n|\mathbf{R}+\mathbf{r}|^3T^3_{ijk}\exp(-\beta^2|\mathbf{R}+\mathbf{r}|^2)-\sum_{\mathbf{R}}\frac{8\beta^5}{\sqrt{\pi}}\frac{\exp(-\beta^2|\mathbf{R}+\mathbf{r}|^2)}{|\mathbf{R}+\mathbf{r}|^2}$$
$$\times\left[\delta_{in}(\mathbf{R}+\mathbf{r})_j(\mathbf{R}+\mathbf{r})_k+\delta_{jn}(\mathbf{R}+\mathbf{r})_i(\mathbf{R}+\mathbf{r})_k+\delta_{kn}(\mathbf{R}+\mathbf{r})_i(\mathbf{R}+\mathbf{r})_j-2(\mathbf{R}+\mathbf{r})_i(\mathbf{R}+\mathbf{r})_j(\mathbf{R}+\mathbf{r})_k(\mathbf{R}+\mathbf{r})_n\left(\beta^2+\frac{1}{|\mathbf{R}+\mathbf{r}|^2}\right)\right]. \tag{A10}$$

For $\mathbf{r}=0$, the sums over $\mathbf{R}$ in Eqs. (A8)–(A10) should be restricted by the constraint $\mathbf{R}\neq 0$. In this case, the sums over the tensors are given by

$$\sum_{\mathbf{R}\neq 0}T^2_{ij}=\tilde{T}^2_{ij}(\mathbf{R}\neq 0)+\frac{4\beta^3}{3\sqrt{\pi}}\delta_{ij}, \tag{A11}$$

$$\sum_{\mathbf{R}\neq 0}T^3_{ijk}=\tilde{T}^3_{ijk}(\mathbf{R}\neq 0), \tag{A12}$$

and

$$\sum_{\mathbf{R}\neq 0}T^4_{ijkn}=\tilde{T}^4_{ijkn}(\mathbf{R}\neq 0)-\frac{8\beta^5}{5\sqrt{\pi}}(\delta_{ij}\delta_{kn}+\delta_{ik}\delta_{jn}+\delta_{jk}\delta_{in}). \tag{A13}$$

[1] M. Parthasarathy and D. Klingenberg, Mater. Sci. Eng., R. **17**, 57 (1996).
[2] W. J. Wen, C. Weisbuch, D. M. Phuong, G. Lu, W. Ge, C. T. Chan, and P. Sheng, Nanotechnology **16**, 598 (2005).
[3] A. Yethiraj and A. van Blaaderen, Nature (London) **421**, 513 (2003).
[4] A. Yethiraj, J. H. J. Thijssen, A. Wouterse, and A. van Blaaderen, Adv. Mater. (Weinheim, Ger.) **16**, 596 (2004).
[5] R. Tao and D. Xiao, Appl. Phys. Lett. **80**, 4702 (2002).
[6] T. J. Chen, R. N. Zitter, and R. Tao, Phys. Rev. Lett. **68**, 2555 (1992).
[7] U. Dassanayake, S. Fraden, and A. van Blaaderen, J. Chem. Phys. **112**, 3851 (2000).
[8] A. Yethiraj, A. Wouterse, B. Groh, and A. van Blaaderen, Phys. Rev. Lett. **92**, 058301 (2004).
[9] R. Tao, J. T. Woestman, and N. K. Jaggi, Appl. Phys. Lett. **55**, 1844 (1989).
[10] R. Tao and J. M. Sun, Phys. Rev. Lett. **67**, 398 (1991).
[11] T. C. Halsey and W. Toor, Phys. Rev. Lett. **65**, 2820 (1990).
[12] W. R. Toor and T. C. Halsey, Phys. Rev. A **45**, 8617 (1992).
[13] R. Friedberg and Y.-K. Yu, Phys. Rev. B **46**, 6582 (1992).
[14] B. Khusid and A. Acrivos, Phys. Rev. E **60**, 3015 (1999).
[15] S. Klapp and F. Forstmann, Phys. Rev. E **60**, 3183 (1999).
[16] R. Tao and J. M. Sun, Phys. Rev. A **44**, R6181 (1991).
[17] J. E. Martin, R. A. Anderson, and C. P. Tigges, J. Chem. Phys. **108**, 3765 (1998).
[18] J. E. Martin, R. A. Anderson, and C. P. Tigges, J. Chem. Phys. **110**, 4854 (1999).
[19] M. Gross and C. Wei, Phys. Rev. E **61**, 2099 (2000).
[20] B. Groh and S. Dietrich, Phys. Rev. E **63**, 021203 (2001).
[21] A.-P. Hynninen and M. Dijkstra, Phys. Rev. Lett. **94**, 138303 (2005).
[22] R. Tao, Phys. Rev. E **47**, 423 (1993).
[23] R. Tao, J. Phys.: Condens. Matter **13**, R979 (2001).
[24] B. Derjaguin and L. Landau, Acta Physicochim. URSS **14**, 633 (1941).
[25] E. J. W. Verwey and J. Th. G. Overbeek, *Theory of the Stability of Lyotropic Colloids* (Elsevier, Amsterdam, 1948).
[26] A.-P. Hynninen and M. Dijkstra, Phys. Rev. E **68**, 021407 (2003).
[27] E. J. Meijer and F. El Azhar, J. Chem. Phys. **106**, 4678 (1997).
[28] F. El Azhar, M. Baus, J.-P. Ryckaert, and E. J. Meijer, J. Chem. Phys. **112**, 5121 (2000).
[29] M. O. Robbins, K. Kremer, and G. S. Grest, J. Chem. Phys. **88**, 3286 (1988).
[30] S. Hamaguchi, R. T. Farouki, and D. H. E. Dubin, Phys. Rev. E **56**, 4671 (1997).
[31] D. Frenkel and B. Smit, *Understanding Molecular Simulations*, 2nd ed. (Academic Press, New York, 2002).
[32] P. P. Ewald, Ann. Phys. **64**, 253 (1921).
[33] Z. Wang and C. Holm, J. Chem. Phys. **115**, 6351 (2001).
[34] D. Frenkel and A. J. C. Ladd, J. Chem. Phys. **81**, 3188 (1984).
[35] A. D. Bruce, N. B. Wilding, and G. J. Ackland, Phys. Rev. Lett. **79**, 3002 (1997).
[36] H. Ma, W. Wen, W. Y. Tam, and P. Sheng, Adv. Phys. **52**, 343 (2003).
[37] G. Arfken, *Mathematical Methods for Physicists*, 2nd ed. (Academic Press, New York, 1970).